Title: Chemogenetic activation of Locus Coeruleus Noradrenergic Neurons Modulates the Default Mode Network

Short title: LC-NE Neurons Modulates the Default Mode Network

Esteban A. Oyarzabal[1-4], Li-Ming Hsu[1-3]*, Manasmita Das[1-3]*, Tzu-Hao Harry Chao[1-3], Jingheng Zhou[6], Sheng Song[1-3], Weiting Zhang[1-3], Kathleen G. Smith[5], Natale R. Sciolino[5], Irina Y. Evsyukova[5], Hong Yuan[2], Sung-Ho Lee[1-3], Guohong Cui[6], Patricia Jensen[5] and Yen-Yu Ian Shih[1-3]*

* Equal contribution

Corresponding author: Yen-Yu Ian Shih (shihy@unc.edu)

Affiliations:

[1]*Center for Animal MRI, University of North Carolina, Chapel Hill, NC, USA*
[2]*Biomedical Research Imaging Center, University of North Carolina, Chapel Hill, NC, USA*
[3]*Department of Neurology, University of North Carolina, Chapel Hill, NC, USA*
[4]*Curriculum in Neurobiology, University of North Carolina, Chapel Hill, NC, USA*
[5]*Developmental Neurobiology Group, Neurobiology Laboratory, NIEHS/NIH, RTP, NC, USA*
[6]*In Vivo Neurobiology Group, Neurobiology Laboratory, NIEHS/NIH, RTP, NC, USA*

Teaser: LC-NE neurons drive NE release, promote neuronal activity and connectivity, but constrict blood vessels in the frontal DMN

Abstract

The default mode network (DMN) of the brain is involved in cognition, emotion regulation, impulsivity, and balancing between internally and externally focused states. Dysregulation of DMN has been implicated in several neurological and neuropsychiatric disorders. In this study, we used functional magnetic resonance imaging (fMRI), positron emission tomography (PET), and spectral fiber-photometry to investigate the selective neuromodulatory effect of norepinephrine (NE)-releasing noradrenergic neurons in the locus coeruleus (LC) on DMN in mice. Chemogenetic-induced LC-NE activation decreased cerebral blood volume (CBV) and glucose uptake, while increasing synchronous low frequency power within the frontal cortices of the DMN. Fiber-photometry results corroborated these findings, showing LC-NE activation induces NE release, enhances calcium-weighted neuronal spiking, and reduces CBV in the anterior cingulate cortex. These data suggest the lack of conventional stimulus-evoked coupling between neuronal activity and CBV in the frontal DMN. We also demonstrated that chemogenetic activation of LC-NE neurons strengthen functional connectivity within the frontal DMN, and this effect is causally mediated by reduced modulatory inputs from retrosplenial and hippocampal regions to the association cortices of the DMN.

Introduction

Functional magnetic resonance imaging (fMRI) has been widely utilized to demonstrate the presence of spatiotemporally consistent intrinsic functional brain networks during resting state. The default mode network (DMN), comprised of prefrontal, orbitofrontal, prelimbic, cingulate, retrosplenial, posterior parietal, temporal association cortices and dorsal hippocampus, is among the most robust intrinsic networks due to its highly synchronized activity in the absence of cognitive tasks or saliency (*1*). The DMN is vulnerable in several neurological and neuropsychiatric disorders (*2*) and is functionally associated with a wide range of behaviors (*3, 4*), integrating interoceptive and exteroceptive information from multiple brain networks (*5*) and maintaining the brain in a semi-vigilant state (*6, 7*). In order to make causal interpretations of behaviorally relevant DMN changes and design network-based interventions for disorders that afflict DMN activity, identifying the modulatory mechanisms controlling the DMN is of paramount importance.

The locus coeruleus (LC), a small nucleus within the pons, is a potential DMN modulator (*8*). LC accounts for large portion of the neuromodulator norepinephrine (NE) released in the brain regions that are considered DMN nodes (*9, 10*). Accumulating evidence suggests that LC-NE may be essential for DMN modulation since: **a)** NE receptors are heavily expressed in all DMN-related brain structures (*9*); **b)** LC-NE can bidirectionally modulate attention reorientation in a dose-dependent manner (*10*); **c)** degeneration of LC-NE neurons and disruption of DMN are coincidently found in depression (*11*), traumatic brain injury (*12*), Parkinson's disease (*13*), Alzheimer's disease (*14*) and aging (*15*); and **d)** pharmacological treatment of pathological LC-NE levels reduces attentional lapses (*16*) and restores DMN integrity in attention deficit hyperactivity

disorder patients (*17*). Despite these findings, the modulatory association between LC-NE and DMN remains circumstantial since pharmacological interventions using NE-related agents inherently result in non-selective binding on dopaminergic, cholinergic and serotonergic receptors (*18, 19*). Furthermore, systemic administration of these agents indiscriminately targets all NE-producing neurons in the brain and sympathetic nervous system, making it difficult determine the role of the LC-NE in modulating the DMN. Though selective manipulation of LC-NE while imaging DMN is currently impossible in humans due to technical and ethical constraints, such studies are feasible in rodent models since structural and functional homologs of the human DMN have been identified in mice (*20-28*) with preserved functional DMN suppression in response to a task-positive whisker stimulation task (*24*).

In this study, we used an established data-driven approach to identify DMN modules (*29*) in mice and an intersectional chemogenetic strategy to selectively and reproducibly activate LC-NE neurons (*30, 31*) to causally determine a circuit model of this modulation. To reveal potential confounders in interpreting the influence of LC-NE on DMN, we measured changes in several fMRI metrics, neuronal calcium activity, and glucose uptake across different spatial and temporal scales. Through modeling the signal dynamics, we revealed the circuit mechanism by which LC-NE activation modulates DMN. Our findings should pave the way towards a better understanding of how large-scale brain networks are mediated by a specific neuromodulatory system.

RESULTS

To selectively and reproducibly activate LC-NE neurons, we used an intersectional chemogenetic approach in which the excitatory G-protein-coupled receptor hM3Dq fused to mCherry is expressed in 99.6% of the anatomically defined LC and a small portion of the dorsal subcoeruleus immediately adjacent to and continuous with the LC (LC-NE/hM3Dq) (*31*) (**Fig. 1**). This population of NE neurons robustly innervates canonical DMN regions including cingulate 1 (Cg1) and retrosplenial (RSC) cortices (**Fig. S1**) (*32*).

To functionally delineate the DMN and study selective NE modulatory effects, we performed *in vivo* CBV-weighted fMRI scans on LC-NE/hM3Dq and littermate control mice (n=9 and 12, respectively) under light isoflurane (~1%) anesthesia using a previously described isotropic echo-planar-imaging protocol (*33*). Though medetomidine is considered the preferred sedative for rodent fMRI (*34*), we avoided its usage since it suppresses NE release (*35*). We collected a 10 min resting-state baseline scan prior to administering a 1 mg/kg intraperitoneal injection of CNO (**Fig. 2A**). This protocol has been shown to activate LC-NE neurons and alter behavior in LC-NE/hM3Dq mice (*30, 31*). Subsequent comparisons were made against littermate controls to account for off-target effects of clozapine-n-oxide (CNO) and/or the back-metabolized clozapine (55). We spatially warped each imaging dataset into the Allen Mouse Common Coordinate Framework (*36*) (**Fig. S2**), functionally parcellated the baseline fMRI data from all subjects (*n*=21) by performing a 100-component independent component analysis (ICA) (*37*) (**Fig. 2, B and C**) and verified their reproducibility (**Fig. S3**). We identified 17 DMN related independent components (ICs) (**Fig. S4A**) according to previous rodent DMN studies (*5, 23, 25, 26, 29*). The areas showing significant temporal correlation associated with the 17 identified DMN ICs were

reconstructed using dual regression (*38*), and one-sample *t*-test was performed to generate the group-level maps representing the connectivity of these ICs. These maps showed high spatial similarity compared to an RSC seed-based connectivity map commonly used to depict DMN (**Fig. S4, B and C**). Louvain community modularity analysis (*39*) clustered the 17 DMN ICs into three distinct modules (Q = 0.10, p<0.01; **Fig. 2D**). A *Frontal* module comprised of pre-limbic/infra-limbic (PrL/IL), lateral orbital (LO), Cg1, and anterior cingulate 2 (aCg2) cortices, an *RSC-HIPP* module comprised of the dorsal hippocampus (HIPP) and posterior Cg2 (pCg2), medial parietal association (MPtA), retrosplenial granular (RSG), retrosplenial dysgranual / visual (RSD / Vis) cortices, and an *Association* module comprised of posterior parietal (PPtC), and auditory (Aud) cortices. No significant difference among the connectivity of DMN ICs were found in the pre-CNO baseline data between LC-NE/hM3Dq and control groups ($P_{FDR\text{-}corrected} > 0.05$, **Fig. S4D**).

Using the *Frontal, RSC-HIPP, and Association* modules ROIs (one-sample *t*-test, $P < 0.0001$) and striatum as a reference region due to sparse LC-NE neuron innervation, we examined how NE release from LC modulates fMRI-derived CBV, regional homogeneity (ReHo) (*40*) and amplitude of low frequency fluctuation (ALFF) (*41*) changes. We compared a 10 min baseline fMRI data prior to administering CNO against data acquired between 20-30 min post-CNO to account for DREADD-induced activity kinetics reported in fMRI (*8, 42-45*) and behavior studies (*30, 31*). CNO-evoked LC-NE activation significantly decreased CBV in all DMN modules in LC-NE/hM3Dq (unpaired *t* test, $P_{FDR\text{-}corrected} < 0.05$) but not in control mice (**Fig. 3A**). LC-NE activation induced CBV changes in the striatum despite the absence of direct NE innervations, possibly due to NE-induced vasoconstriction upstream of the watershed arterioles that perfuse the striatum (*46*). While the CBV change appeared less specific, the ReHo (**Fig. 3B**) and ALFF (**Fig. 3C**) changes were

more localized, and the increase of these signals contradicted the intuitive interpretation of CBV, implying a possible increase of synchronous, low-frequency activity in the *Frontal* and *RSC-HIPP* DMN modules by LC-NE. Specifically, LC-NE activation enhanced ALFF changes within 0.01 and 0.05 Hz band frequencies (unpaired *t* test, $P_{FDR\text{-}corrected} < 0.05$; **Fig. S5A**).

To validate these fMRI findings, we employed spectral fiber-photometry (**Fig. 4A**) in LC-NE/hM3Dq (n=5) and control mice (n=4). We virally expressed a genetically engineered $NE_{2.1}$ sensor (71) and a red-shifted jRGECO1a calcium activity sensor (72) under the pan-neuronal human Synapsin-1 (hSyn) promoter in the Cg1 of the *Frontal* DMN module (**Fig. 4B**), where the effects of LC-NE activation were most robust. Additionally, we intravenously administered a CY5-conjugated Dextran far-red fluorescent dye to measure CBV (**Fig. S6**), allowing us to simultaneously detect changes in synaptic NE release, neuronal activity-mediated calcium influx and CBV in Cg1 (**Fig. 4C**). After CNO administration, we observed significant increases in NE release (unpaired t test, $P_{\text{FDR-corrected}} < 0.05$; **Fig. 4D**), decreases in CBV (unpaired t test, $P_{\text{FDR-corrected}} < 0.05$; **Fig. 4E**), and an increase in neuronal activity (unpaired t test, $P_{\text{FDR-corrected}} < 0.05$; **Fig. 4F**) in LC-NE/hM3Dq mice compared to controls. Notably, the number of calcium spikes also increased significantly following CNO administration (unpaired t test, $P_{\text{FDR-corrected}} < 0.05$; **Fig. 4G**), showing a hallmark of NE by tuning the signal-to-noise ratio of downstream neuronal firing (73). These findings corroborate well with our fMRI results (**Fig. 3**) and indicate that driving LC-NE release can concurrently induce regional vasoconstriction while enhancing neuronal excitability in Cg1. Given that fMRI does not directly measure neuronal activity, these results highlight the importance of cautiously interpreting fMRI-derived DMN results when NE is involved, as inferring neuronal activity by direct fMRI signal changes in this case may be erroneous.

We also examined the effect of NE on brain glucose uptake in a subset of LC-NE/hM3Dq (n=5) and control (n=5) mice using an established [^{18}F]-fluorodeoxyglucose (FDG)-PET protocol (*47*). Interestingly, we found CNO-induced LC-NE activation significantly decreased glucose uptake in all three DMN modules (paired *t* test, $P_{FDR\text{-}corrected} < 0.001$), but not in control subjects (**Fig. 5** and **S7**). Though there are mixed findings on how NE alters glucose uptake (*48-53*), most studies using pharmacology to enhance NE release showed suppressed glucose uptake (*48-53*) by shifting astrocyte metabolism to preferentially utilize glycogen reserves (*52, 53*). Taken together, these findings suggest additional caution needs to be considered for FDG-PET data interpretation when triggering NE release.

To shed light on how selective NE release modulates DMN connectivity and network properties, we examined FC changes within and between *Frontal*, *RSC-HIPP*, and *Association* DMN modules in LC-NE/hM3Dq (n=9) and control mice (n=12). We found that CNO significantly enhanced FC within *Frontal* ($F_{(2,26)}$=5.2, $P_{FDR\text{-}corrected} < 0.05$) and between *Frontal* and *Association* modules ($F_{(2,26)}$ =6.0, $P_{FDR\text{-}corrected} < 0.05$) of the DMN in LC-NE/hM3Dq, but not in control mice (**Fig. 6, A and B**). Notably, the high intramodular connectivity characterized by within-module degree (WD), quantifies the level of connectivity of nodes within a module, indicating that Cg1 and RSC serve as provincial hubs for the *Frontal* and *RSC-HIPP* modules of the DMN, respectively (**Fig. S8, A and B**). The high intermodular connectivity characterized by partition coefficient (PC), estimates the level of interactions with nodes of other modules, indicating aCg2 of the *Frontal* module serves as a connector hub throughout the entire DMN and may control the FC between *Frontal* and other modules (**Fig. S8, A and B**). Given the putative causal control of the anterior insular cortex (AI) on the *Frontal* module of the DMN (*54, 55*), we also examined the effects of

LC-NE activation on their FC changes and found that CNO-evoked activation significantly enhanced anti-correlation between AI and DMN frontal module (**Fig. S8, C and D**).

To further unravel the causal influences on FC in DMN modules by LC-NE activation, we conducted a dynamic causal modeling (DCM) analysis (*56*) and found LC-NE activation significantly reduced effective connectivity (EC) from *RSC-HIPP* to the *Association* module following LC-NE activation (paired *t*-test, $P_{FDR\text{-}corrected} < 0.05$, **Fig. 7A**), while no change was detected in the littermate controls (**Fig. S9A**). Analyses of the co-activation patterns (CAPs) (*7*) may support these findings, as the CAP representing distinct *RSC-HIPP* and *Association* states was also suppressed following LC-NE activation (**Fig. S9B-D**). Together with the robust NE modulatory effects in the *Frontal* module, these findings prompted us to conduct a mediation analysis to determine the origin of the FC changes in the *Frontal* module. Using a general linear model (GLM), we demonstrated that the reduction in EC observed from *RSC-HIPP* to the *Association* module causally manipulates the FC changes within the *Frontal* module (coefficient = -0.53±0.13, $P < 0.001$; **Fig. 7B**). When we incorporated the FC increases between the *Frontal* and *Association* modules as a mediator, we observed a full mediation effect (*57*) of the reduced EC to the *Frontal* module FC changes while the direct relationship between the reduced EC from *RSC-HIPP* to the *Association* module and the increased FC within *Frontal* module became insignificant (coefficient = -0.26±0.13, N.S.). The Sobel test (*58*) further indicated the significant mediation effect (Sobel z = -2.02, $P < 0.05$; **Fig. 7B**). In contrast, we did not observe the reduced EC from the *RSC-HIPP* to *Association* module being mediated by the FC increases between *Frontal* and *Association* modules (**Fig. S10**). Collectively, these findings indicate that LC-NE activation modulates the DMN by **1)** strengthening FC within the *Frontal* module, **2)** strengthening FC between *Frontal* and

Association modules, and **3)** reducing *RSC-HIPP* control over the *Association* module, which causally alters *Frontal* module FC, while the FC between *Frontal* and *Association* modules serves as a key mediator.

DISCUSSION

The Mouse DMN

The mouse DMN has been observed by fMRI, optical imaging and functional ultrasound (*20-28*). Most studies analyzing the mouse DMN using ICA or seed-based connectivity analyses reported consistent DMN architectures that are homologous to the human DMN. A multi-center study compiled by Grandjean *et al.* analyzed several resting-state mouse fMRI datasets acquired under various conditions (e.g. magnetic field strengths, coils, imaging parameters, and anesthesia protocols) and generated a group ICA atlas delineating mouse brain connectivity (*23*). The results pulled three DMN modules that include prefrontal, cingulate/retrosplenial, and temporal association areas. Similar to those findings, analysis of our data revealed three modules including *Frontal*, *RSC-HIPP*, and *Association* modules, where the *Frontal* and *RSC-HIPP* modules included prefrontal and posterior cingulate components, respectively (**Fig. 2C**). It should be noted that the involvement of the hippocampus in the mouse DMN remain disputed due to the lack of direct anatomical projections (*23, 25, 26*). This study includes hippocampus as part of the DMN because we followed recent studies dissecting the DMN constituents in rats (*5, 29*) and humans (*3, 59*). Additionally, several unbiased hierarchical clustering analyses, including our own, functionally classified the hippocampus as part of the DMN (*60*) and lend further support to the validity of the DMN modules used for the analysis in this study.

LC-NE Modulates DMN Activity

Several research groups have pioneered chemogenetic fMRI (*8, 45, 61, 62*) and PET (*63*) approaches to selectively map the influence of neurotransmitters on brain networks. Our experimental design employing and intersectional chemogenetic mouse line presented a unique opportunity to investigate functional DMN modulation by using a strategy that permits noninvasive and reproducible activation of LC-NE neurons. We demonstrated that chemogenetic activation of LC-NE neurons showed significant reduction in CBV and glucose uptake among all three DMN modules compared to littermate controls (**Fig. 3 and 5**). Utilizing littermate controls is essential for rigor in chemogenetic studies (*64*) since off-target binding of CNO or clozapine through reverse-metabolism of CNO may occur (*65*). Of note, the modulatory effect seen in the striatum suggest that LC-NE's influence on these metrics may extend beyond the brain regions receiving direct innervation from LC-NE neurons.

While both fMRI and fiber-photometry corroborated the CBV reduction finding in the *Frontal* DMN module following activation of LC-NE neurons, we observed a concurrent increase of synchronous low frequency activity as measured by ReHo, ALFF, and changes in calcium activity in our experimental condition (**Fig. 4, D-G**). The most straightforward interpretation of the fMRI data based on well-documented neurovascular coupling rule (*66*) does not apply, likely due to the potent vasoconstrictive properties of NE (*67, 68*). It is not surprising that the neuromodulatory effect induced by NE release appears inconsistent in the literature owing to various brain states and basal firing rate examined, as well as the distinct experimental approaches utilized to promote NE release (*8, 69-72*). The literature also shows mixed findings regarding the effects of NE on both cerebral hemodynamics and metabolism, possibly because

common pharmacological agents used to induce NE release suffer from differential actions on NE receptor subtypes and non-selective binding that can either increase (*73*) or decrease perfusion (*67, 68*) and increase (*48, 49*) or decrease glucose metabolism (*50, 51*). Of note, the changes observed in glucose metabolism following LC-NE stimulation could also be attributed to dose-dependent shifting of glial metabolism, whereby a high NE level shifts metabolism to preferentially glycogen deposits from blood glucose (*52, 53*). Unlike many studies that use pharmacological manipulations of NE release, our chemogenetic approach coupled with multimodal measurement of NE, neuronal activity, and CBV revealed an effect of NE in increasing synchronized low frequency activity, strengthening neuronal firing, and decreasing CBV. This has significant implications when using fMRI to interpret DMN neuronal activity, as "deactivation" of raw fMRI signal caused by LC-NE activation may not necessarily represent reduced DMN neuronal activity.

Nevertheless, enhanced LC-NE release in human fMRI studies using atomoxetine (*69, 74*) and pupillary dilation under dark settings (*75*) support that higher levels of tonic LC-NE release enhance synchrony within local rather than distant brain regions, and that NE shifts resting-state activity from widely distributed patterns to tighter clustered patterns dominated by the strongest input networks. This interpretation aligns well with our findings showing enhanced ReHo within the *Frontal* DMN module following CNO-evoked LC-NE activation. Our ALFF results show LC-NE activation enhanced low-frequency power of the *Frontal* DMN that was restricted to a frequency band ranging from 0.01 to 0.05 Hz—a range associated with robust changes in human DMN (*76*). Alterations in the power within this sub frequency band of ALFF also plays a vital role in attention

reorientation during visual-motor attentional tasks (*76*), which has also been linked to changes in cortical NE levels (*77*).

LC-NE Modulates DMN Connectivity

LC-NE enhanced FC within the *Frontal* module and between *Frontal* and *Association* modules. In agreement with our finding, a seminal study virally transfecting hM3Dq via the *Dbh* promotor into the LC found significant FC enhancement in the Cg1, Cg2 and RSC following chemogenetic stimulation (*8*). The increased FC within the *Frontal* modules of the DMN aligns with the findings that spontaneous rises in tonic LC-NE release, as detected by changes in pupil dilation, disrupts FC network integration and shift towards segregated network topologies with enhanced temporal correlation within local brain networks (*75, 78*). Furthermore, our findings show LC-NE activation enhances the anti-correlation between the *Frontal* DMN module and the AI (**Fig. S8, C and D**), a key node of the salience network that may causally suppress DMN (*54*). This enhanced polarization among networks also supports the plausible mechanism by which NE-targeting pharmacological agents like atomoxetine, clonidine and guanfacine are effective in treating ADHD patients since they strengthen the FC within the *Frontal* DMN module, resulting in improved attention (*79, 80*). Additionally, abnormally heightened FC in *Frontal* DMN regions have been associated with anxiety and depression (*81, 82*), which coincide with anxiety-like behavioral phenotypes such as reduced locomotor activity when placed in a novel environment and anhedonia following chemogenetic-evoked LC-NE activation in awake mice (*30*). Optogenetically driving LC-NE neuronal activation at tonic frequencies above 5 Hz have been shown to entirely suppress novelty-seeking behavior and result in freezing (*83*). Considering our findings of strengthened *Frontal* DMN connectivity, such behavior is likely associated with the

shift towards a DMN-dominated brain state. It is also possible that activation of lower affinity adrenergic receptors signaling induces aversive affective states (*84*).

Our DCM and mediation analyses show that enhanced *Frontal* module connectivity in the DMN was causally manipulated by reducing *RSC-HIPP* control of the *Association* module, with the connectivity between the *Association* and *Frontal* modules serving as a key mediator. These findings reveal a new understanding of how LC-NE activation controls the signaling cascades within DMN modules and achieves its control of the *Frontal* cortical regions, which are among the most well-studied projection targets of LC-NE due to their importance in shaping multiple behaviors (*84*). LC-NE neuronal loss and the subsequent depletion of cortical NE levels are widely considered to be among the first sites of neurodegeneration in Parkinson's and Alzheimer's disease (*85*), resulting in behavioral pathologies linked to alterations in DMN such as delayed attention shifting (*86, 87*), enhanced mind-wandering (*88*) and reduced cognitive and emotional processing of sensory information (*87, 88*). Optogenetically-evoked LC-NE activation at lower tonic frequencies into prefrontal and orbitofrontal cortices enhances stimulus and goal-directed attention with decreased impulsivity (*89*). Conversely, the suppression of LC-NE activation exacerbates distractibility and impulsivity (*89*), similar to that observed in Parkinson's and Alzheimer's disease patients (*88*). Taken together, alterations within *Frontal* and between *Frontal* and *RSC-HIPP* DMN modules have potential to serve as early biomarkers for pathophysiological changes in LC-NE neurons. Our circuit-level findings could also pave the way towards novel targets to causally control the *Frontal* DMN via the *RSC-HIPP* module when LC neurons have degenerated, such that the behavioral traits relevant to the *Frontal* DMN may be restored when endogenous NE is pathologically diminished.

MATERIAL AND METHODS

Animals

All animal procedures were performed in strict compliance with ethical regulations for animal research and approved by the Institutional Animal Care and Use Committee of the University of North Carolina at Chapel Hill. *En1*^{cre} (*90*), *Dbh*^{Flpo} (*32*), *RC::FL-hM3Dq (31)*, and *RC::FLTG* (*91*) mouse colonies are maintained on a C57BL/6J background. Male and female triple transgenic animals were generated at the National Institute of Environmental Health Sciences by crossing *En1*^{cre} mice to double transgenic *Dbh*^{Flpo}*; RC::FL-hM3Dq* or *Dbh*^{Flpo}*; RC::FLTG* mice. Single- and double-transgenic littermates served as controls. All animals were maintained on a 12/12 h light-dark cycle with access to food and water *ad libitum*.

CBV-fMRI acquisition

For fMRI studies, LC-NE (n=9) and control mice (n=12) were initially anesthetized using 2-3% isoflurane and maintained under light anesthesia (1% isoflurane) while preserving physiological homeostasis. All MRI experiments were performed on a Bruker BioSpec 9.4-Tesla, 30 cm bore system (Bruker BioSpin Corp., Billerica, MA) with ParaVision 6.0.1 on an AVANCE II console. An RRI BFG 150/90 gradient insert (Resonance Research Inc., Billerica, MA) paired with a Copley C700 gradient amplifier (Copley Controls Corp., Canton, MA) were used for all experiments. A 72 mm volume coil was used as the transmitter and quadrature mouse brain coil was used as the receiver (Bruker BioSpin Corp., Billerica, MA). Magnetic field homogeneity was optimized first by global shimming, followed by local second-order shims using a MAPSHIM protocol. All CBV-fMRI data were acquired using a 2D multi-slice, single-shot, gradient-echo echo-

planar imaging sequence: TR (repetition time) = 3000 ms, TE (echo time) = 7.9 ms, bandwidth = 250 kHz, flip angle = 70 degrees, FOV (field of view) = 19.2 x 19.2 mm^2, matrix size = 64 x 64, slice number =26, slice thickness =0.3 mm, resulting in isotropic voxel size of 0.3 mm^3. Subjects were continuously scanned for 40 min with a 1 mg/kg dose of CNO administered via an intraperitoneal catheter 10 min after scan onset. CBV-weighted fMRI was achieved by a bolus dose of an in-house developed iron oxide nanoparticles (30 mg Fe/kg, i.v.) (*92*). Rectal body temperatures were continuously maintained at 37±0.5°C by a temperature controller (Oakton Temp9500, Cole-Parmer, Vernon Hills, IL, USA) coupled to a circulating water bath (Haake S13, Thermo Scientific, Waltham, MA, USA) that heats the MRI mouse cradle. Respiration was monitored through a pneumatic pillow (Respiration/EEG Monitor, SA Instruments, Stony Brook, NY, USA) and maintained between 90-110 breaths/min.

fMRI data analysis

Pre-processing of images: All fMRI data were first corrected for slice timing and motion using AFNI. Brain data were isolated for each subject using a U-Net deep-learning skull stripping tool (*93*) by averaging temporal data into a single volume. Skull-stripped data were spatially normalized to our EPI template using ANTs. Additionally, de-spiking, ICA de-noising, and nuisance variable regression of the six motion parameters estimated from motion correction and the CSF signal extracted using a mask of the major brain ventricles. Dataset were then smoothed using a Gaussian kernel with full width half maximum (FWHM) at 0.6 mm, de-trended, and temporally filtered by applying a high-pass filter between > 0.01 Hz. Datasets underwent quality control by measuring frame wise displacement (FD), temporal SNR (tSNR), and DVARS (temporal derivative

of the root mean squared variance over voxels). A detailed description of the preprocessing pipeline (*33, 94*) can be found in the **Supplementary Methods**.

ICA and modularity analyses: MRI data were decomposed into 100 functional components using baseline data from all subjects via a group-level ICA (FSL MELODIC). ICA spatial maps were back-reconstructed for each subject to estimate subject-specific temporal components and associated spatial maps using dual-regression analysis (*38*) and a t-test was performed to generate group component maps. Individual time courses from 17 pre-selected DMN nodes to were extracted from first stage of dual-regression and the Fisher z-transformed Pearson correlation were computed among all node pairs to form a correlation matrix. To keep the strongest connections without isolated nodes, the z-threshold = 0.26 (connection density = 48%) was set in the mean FC matrix across all subjects. Functional modules of the DMN were parcellated using Louvain community detection algorithm (*95*). The modularity analysis method is detailed in the **Supplementary Methods**.

ReHo and ALFF analyses of DMN modules: ReHo is a voxelwise analysis to determine local synchronization of fMRI signal among all brain regions (*96*). Higher ReHo scores typically represent greater neuronal coherence and centrality within nodes but does not necessarily equate to higher neuronal activity (*96*). ALFF is a voxelwise technique to calculate the total power of regional neuronal activity within 0.01-0.1 Hz (*96*). Overlapping regions that share high ALFF and ReHo scores are thought to have enhanced synchronization of low frequency neuronal activity (*96*).

FC analysis within and between DMN modules: Within- and between-module connectivity was defined as the average of FC across node pairs within or between the identified DMN

modules. We conducted network-based statistics (NBS) (*97*) to investigate the significant connection changes. For each comparison, a primary component-forming threshold ($p<0.05$, uncorrected) was applied to form a set of supra-threshold edges and all the remaining connected subnetworks in the matrix were then evaluated under the null hypothesis of random group membership (5,000 permutations).

DCM analysis: We specified a DCM model with full connectivity consisting of three modules from DMN. After extracting the fMRI time series from the DMN modules through dual-regression analysis, we used spectral DCM in SPM12 (*98*) to estimate pairwise EC among the DMN modules and constructed a directed and weighted graph (representing an EC network) for each subject.

Mediation analysis: We applied serial-multiple mediation analysis model using the structural equation modeling method (*99*) in AMOS 17.0 (SPSS Inc., Chicago, IL, USA) to uncover underlying functional pathways within DMN. Specifically, we first estimated the direct relationships between dependent variable (EC from *RSC-HIPP* module to *Association* module) and independent variable (FC within *Frontal* module). Then, in a mediation model, the FC between *Association* and *Frontal* module was added as a mediator. In this context, full mediation occurs when the relationship between the independent variable and the dependent variable is no longer significant with the inclusion of a mediator variable (*57*). For each pathway, we utilized the bootstrapping test for 1,000 times to test the significance. Finally, the mediation effect was evaluated using the Sobel test (*100*) detailed in the **Supplementary Methods**.

FDG PET procedure

Mice were fasted 12 h prior to undergoing ^{18}F-FDG PET scans to reduce variability in blood glucose levels that could alter ^{18}F-FDG uptake (117). Static PET scans were collected on the same cohort of animal over two scan sessions using LC-NE/hM3Dq (n=5) and control (n=6) mice to represent sham-treated baseline or CNO-treated condition. Mice were briefly anesthetized under 1-3% isoflurane and injected with either a saline + DMSO vehicle or CNO dissolved in DMSO (1 mg/kg, i.p.) and subsequently received an i.v. injection of ~0.2 mCi of ^{18}F-FDG after 5 min. Mice were recovered in their home cages for a 45 min uptake period. Mice subsequently were anesthetized with isoflurane (2%) and underwent a 10 min CT and 20 min PET scan on a small animal PET/CT scanner (Argus-2R, Sedecal, Madrid, Spain). PET data were reconstructed using the 2D ordered subset expectation maximization (OSEM) algorithm expressed in standardized uptake values (SUV) and normalized using muscle uptake of ^{18}F-FDG using PMOD (PMOD Technologies LLC, Zurich, Switzerland). Data were represented as % changes in SUV between vehicle and CNO scans.

Fiber-photometry procedure

Surgical AAV microinjection and fiber implantation: LC-NE (n=5) and control (n=5) mice were microinjected 0.3 µl of AAV5-hsyn-$NE_{2.1}$ (h-N01, WZ Biosciences) and 0.5 µl of AAV9-hsyn-jRGECO1a (100854, Addgene) to the left Cg1 (AP=2.2mm, ML=0.2mm, DV=-1.6mm). The $NE_{2.1}$ (a green fluorescent norepinephrine sensor) and the jRGECO1a (a red-shifted intracellular calcium sensor) were used for determining the NE release and neuronal activity, respectively. An optic

fiber was implanted 0.3 mm above the injection site and imbedded to the skull using cement (C&B Metabond, S380, Parkell).

Fiber-photometry recording: All recordings began at least four weeks after surgery. CY5-conjugated Dextran fluorescent dye (20 mg/kg, R-FN-006, RuixiBio) was injected intravenously for CBV measurements. Animals were prepared and maintained under the same conditions as fMRI experiments. A spectral fiber-photometry system capable of recording $NE_{2.1}$, jRGECO1a, and CY5 signals simultaneously was used for the experiment. Detailed methods can be found in the **Supplementary Methods**.

Immunohistology procedure

Mice were deeply anesthetized with sodium pentobarbital and transcardially perfused with 0.1 M phosphate buffered saline (PBS) followed by 4% PFA. Brains were post-fixed overnight by immersion in 4% PFA at 4°C. Following a rinse in PBS, brains were cryoprotected in 30% sucrose in PBS and embedded in Tissue Freezing Medium. 40 µm free-floating coronal cryosections were collected in PBS and processed for immunohistochemistry according to previously published protocol (*32, 91*). In brief, free-floating sections were blocked in 5% normal goat serum in PBS with 0.1 % Triton X-100) for 1 h prior to incubating in primary antibody overnight at 4°C. Primary antibodies against mCherry (EST202, Kerafast), GFP (AB13970, Abcam) and NET (1447-NET, Phosphosolutions). Sections were washed in PBS 3x and incubated for 2 h in the secondary antibody the following day. Secondary antibodies were Alexa Fluor 488, 568, 648 (Invitrogen). Sections were mounted onto glass slides and imaged on a Zeiss LSM 880 inverted confocal microscope.

Data availability. All MRI, PET, and photometry data from this study are openly available on [Open Neuro link].

Acknowledgements. This research was supported by the Extramural Research Programs of US National Institutes of Health, NINDS (R01NS091236), NIMH (R01MH126518, R01MH111429, RF1MH117053), NIAAA (P60AA011605 and U01AA020023), and NICHD (P50HD103573) to Y.Y.I.S and the Intramural Research Program of the US National Institutes of Health, National Institute of Environmental Health Sciences (ZIA-ES102805 to P.J. and 1ZIAES103310 to G.C.). We thank the members of the UNC Center for Animal MRI for discussion and Drs. Fulton Crews and Zoe McElligott for their inputs to this study. We thank UNC Small Animal Imaging Core Facility staff Jon Frank and Joseph Merrill for their assistance in PET data acquisition.

Author contributions. E.A.O., M.D., and Y.I.S. designed the study. E.A.O and M.D. collected the imaging data. E.A.O., L.M.H and S.L. analyzed the imaging data. J.Z. and G.C. performed the viral injections and fiber implantation. E.A.O., T.H.C. and W.Z. collected and analyzed the fiber photometry data. K.S. processed and K.S. and P.J. analyzed the histology data. N.S., I.E. and P.J. developed and shared the transgenic mice. E.A.O., L.M.H., P.J. and Y.I.S. wrote the manuscript with input from all authors.

Additional information. Supplementary information accompanies this paper at [link].

References

1. M. E. Raichle, The brain's default mode network. *Annu Rev Neurosci* **38**, 433-447 (2015).

2. R. L. Buckner, J. R. Andrews-Hanna, D. L. Schacter, The brain's default network: anatomy, function, and relevance to disease. *Ann N Y Acad Sci* **1124**, 1-38 (2008).
3. K. Christoff, Z. C. Irving, K. C. Fox, R. N. Spreng, J. R. Andrews-Hanna, Mind-wandering as spontaneous thought: a dynamic framework. *Nat Rev Neurosci* **17**, 718-731 (2016).
4. J. R. Andrews-Hanna, J. S. Reidler, J. Sepulcre, R. Poulin, R. L. Buckner, Functional-anatomic fractionation of the brain's default network. *Neuron* **65**, 550-562 (2010).
5. H. Lu, Q. Zou, H. Gu, M. E. Raichle, E. A. Stein, Y. Yang, Rat brains also have a default mode network. *Proc Natl Acad Sci U S A* **109**, 3979-3984 (2012).
6. P. Lin, Y. Yang, J. Gao, N. De Pisapia, S. Ge, X. Wang, C. S. Zuo, J. Jonathan Levitt, C. Niu, Dynamic Default Mode Network across Different Brain States. *Sci Rep* **7**, 46088 (2017).
7. D. Gutierrez-Barragan, M. A. Basson, S. Panzeri, A. Gozzi, Infraslow State Fluctuations Govern Spontaneous fMRI Network Dynamics. *Curr Biol* **29**, 2295-2306 e2295 (2019).
8. V. Zerbi, A. Floriou-Servou, M. Markicevic, Y. Vermeiren, O. Sturman, M. Privitera, L. von Ziegler, K. D. Ferrari, B. Weber, P. P. De Deyn, N. Wenderoth, J. Bohacek, Rapid ReconFiguration of the Functional Connectome after Chemogenetic Locus Coeruleus Activation. *Neuron* **103**, 702-718 e705 (2019).
9. R. L. van den Brink, T. Pfeffer, T. H. Donner, Brainstem Modulation of Large-Scale Intrinsic Cortical Activity Correlations. *Front Hum Neurosci* **13**, 340 (2019).
10. S. J. Sara, S. Bouret, Orienting and reorienting: the locus coeruleus mediates cognition through arousal. *Neuron* **76**, 130-141 (2012).
11. X. Zhu, Q. Zhu, H. Shen, W. Liao, F. Yuan, Rumination and Default Mode Network Subsystems Connectivity in First-episode, Drug-Naive Young Patients with Major Depressive Disorder. *Sci Rep* **7**, 43105 (2017).
12. D. J. Sharp, C. F. Beckmann, R. Greenwood, K. M. Kinnunen, V. Bonnelle, X. De Boissezon, J. H. Powell, S. J. Counsell, M. C. Patel, R. Leech, Default mode network functional and structural connectivity after traumatic brain injury. *Brain* **134**, 2233-2247 (2011).
13. M. Pievani, N. Filippini, M. P. van den Heuvel, S. F. Cappa, G. B. Frisoni, Brain connectivity in neurodegenerative diseases--from phenotype to proteinopathy. *Nat Rev Neurol* **10**, 620-633 (2014).
14. P. Wang, B. Zhou, H. Yao, Y. Zhan, Z. Zhang, Y. Cui, K. Xu, J. Ma, L. Wang, N. An, X. Zhang, Y. Liu, T. Jiang, Aberrant intra- and inter-network connectivity architectures in Alzheimer's disease and mild cognitive impairment. *Sci Rep* **5**, 14824 (2015).
15. B. B. Biswal, M. Mennes, X. N. Zuo, S. Gohel, C. Kelly, S. M. Smith, C. F. Beckmann, J. S. Adelstein, R. L. Buckner, S. Colcombe, A. M. Dogonowski, M. Ernst, D. Fair, M. Hampson, M. J. Hoptman, J. S. Hyde, V. J. Kiviniemi, R. Kotter, S. J. Li, C. P. Lin, M. J. Lowe, C. Mackay, D. J. Madden, K. H. Madsen, D. S. Margulies, H. S. Mayberg, K. McMahon, C. S. Monk, S. H. Mostofsky, B. J. Nagel, J. J. Pekar, S. J. Peltier, S. E. Petersen, V. Riedl, S. A. Rombouts, B. Rypma, B. L. Schlaggar, S. Schmidt, R. D. Seidler, G. J. Siegle, C. Sorg, G. J. Teng, J. Veijola, A. Villringer, M. Walter, L. Wang, X. C. Weng, S. Whitfield-Gabrieli, P. Williamson, C. Windischberger, Y. F. Zang, H. Y. Zhang, F. X. Castellanos, M. P. Milham, Toward discovery science of human brain function. *Proc Natl Acad Sci U S A* **107**, 4734-4739 (2010).
16. A. Smith, D. Nutt, Noradrenaline and attention lapses. *Nature* **380**, 291 (1996).

17. E. Hoekzema, S. Carmona, J. A. Ramos-Quiroga, V. Richarte Fernandez, R. Bosch, J. C. Soliva, M. Rovira, A. Bulbena, A. Tobena, M. Casas, O. Vilarroya, An independent components and functional connectivity analysis of resting state fMRI data points to neural network dysregulation in adult ADHD. *Hum Brain Mapp* **35**, 1261-1272 (2014).
18. F. P. Bymaster, J. S. Katner, D. L. Nelson, S. K. Hemrick-Luecke, P. G. Threlkeld, J. H. Heiligenstein, S. M. Morin, D. R. Gehlert, K. W. Perry, Atomoxetine increases extracellular levels of norepinephrine and dopamine in prefrontal cortex of rat: a potential mechanism for efficacy in attention deficit/hyperactivity disorder. *Neuropsychopharmacology* **27**, 699-711 (2002).
19. A. Gobert, J. M. Rivet, L. Cistarelli, C. Melon, M. J. Millan, Alpha2-adrenergic receptor blockade markedly potentiates duloxetine- and fluoxetine-induced increases in noradrenaline, dopamine, and serotonin levels in the frontal cortex of freely moving rats. *J Neurochem* **69**, 2616-2619 (1997).
20. J. M. Stafford, B. R. Jarrett, O. Miranda-Dominguez, B. D. Mills, N. Cain, S. Mihalas, G. P. Lahvis, K. M. Lattal, S. H. Mitchell, S. V. David, J. D. Fryer, J. T. Nigg, D. A. Fair, Large-scale topology and the default mode network in the mouse connectome. *Proc Natl Acad Sci U S A* **111**, 18745-18750 (2014).
21. M. P. Vanni, A. W. Chan, M. Balbi, G. Silasi, T. H. Murphy, Mesoscale Mapping of Mouse Cortex Reveals Frequency-Dependent Cycling between Distinct Macroscale Functional Modules. *J Neurosci* **37**, 7513-7533 (2017).
22. J. Grandjean, V. Zerbi, J. H. Balsters, N. Wenderoth, M. Rudin, Structural Basis of Large-Scale Functional Connectivity in the Mouse. *J Neurosci* **37**, 8092-8101 (2017).
23. J. Grandjean, C. Canella, C. Anckaerts, G. Ayranci, S. Bougacha, T. Bienert, D. Buehlmann, L. Coletta, D. Gallino, N. Gass, C. M. Garin, N. A. Nadkarni, N. S. Hubner, M. Karatas, Y. Komaki, S. Kreitz, F. Mandino, A. E. Mechling, C. Sato, K. Sauer, D. Shah, S. Strobelt, N. Takata, I. Wank, T. Wu, N. Yahata, L. Y. Yeow, Y. Yee, I. Aoki, M. M. Chakravarty, W. T. Chang, M. Dhenain, D. von Elverfeldt, L. A. Harsan, A. Hess, T. Jiang, G. A. Keliris, J. P. Lerch, A. Meyer-Lindenberg, H. Okano, M. Rudin, A. Sartorius, A. Van der Linden, M. Verhoye, W. Weber-Fahr, N. Wenderoth, V. Zerbi, A. Gozzi, Common functional networks in the mouse brain revealed by multi-centre resting-state fMRI analysis. *Neuroimage* **205**, 116278 (2020).
24. J. Ferrier, E. Tiran, T. Deffieux, M. Tanter, Z. Lenkei, Functional imaging evidence for task-induced deactivation and disconnection of a major default mode network hub in the mouse brain. *Proc Natl Acad Sci U S A* **117**, 15270-15280 (2020).
25. L. Coletta, M. Pagani, J. D. Whitesell, J. A. Harris, B. Bernhardt, A. Gozzi, Network structure of the mouse brain connectome with voxel resolution. *Sci Adv* **6**, (2020).
26. J. D. Whitesell, A. Liska, L. Coletta, K. E. Hirokawa, P. Bohn, A. Williford, P. A. Groblewski, N. Graddis, L. Kuan, J. E. Knox, A. Ho, W. Wakeman, P. R. Nicovich, T. N. Nguyen, C. T. J. van Velthoven, E. Garren, O. Fong, M. Naeemi, A. M. Henry, N. Dee, K. A. Smith, B. Levi, D. Feng, L. Ng, B. Tasic, H. Zeng, S. Mihalas, A. Gozzi, J. A. Harris, Regional, Layer, and Cell-Type-Specific Connectivity of the Mouse Default Mode Network. *Neuron*, (2020).
27. Y. Ma, M. A. Shaik, M. G. Kozberg, S. H. Kim, J. P. Portes, D. Timerman, E. M. Hillman, Resting-state hemodynamics are spatiotemporally coupled to synchronized and

symmetric neural activity in excitatory neurons. *Proc Natl Acad Sci U S A* **113**, E8463-E8471 (2016).
28. B. R. White, A. Q. Bauer, A. Z. Snyder, B. L. Schlaggar, J. M. Lee, J. P. Culver, Imaging of functional connectivity in the mouse brain. *PLoS One* **6**, e16322 (2011).
29. L. M. Hsu, X. Liang, H. Gu, J. K. Brynildsen, J. A. Stark, J. A. Ash, C. P. Lin, H. Lu, P. R. Rapp, E. A. Stein, Y. Yang, Constituents and functional implications of the rat default mode network. *Proc Natl Acad Sci U S A* **113**, E4541-4547 (2016).
30. Y. W. Chen, M. Das, E. A. Oyarzabal, Q. Cheng, N. W. Plummer, K. G. Smith, G. K. Jones, D. Malawsky, J. L. Yakel, Y. I. Shih, P. Jensen, Genetic identification of a population of noradrenergic neurons implicated in attenuation of stress-related responses. *Mol Psychiatry* **24**, 710-725 (2019).
31. N. R. Sciolino, N. W. Plummer, Y. W. Chen, G. M. Alexander, S. D. Robertson, S. M. Dudek, Z. A. McElligott, P. Jensen, Recombinase-Dependent Mouse Lines for Chemogenetic Activation of Genetically Defined Cell Types. *Cell Rep* **15**, 2563-2573 (2016).
32. S. D. Robertson, N. W. Plummer, J. de Marchena, P. Jensen, Developmental origins of central norepinephrine neuron diversity. *Nat Neurosci* **16**, 1016-1023 (2013).
33. S. H. Lee, M. A. Broadwater, W. Ban, T. W. Wang, H. J. Kim, J. S. Dumas, R. P. Vetreno, M. A. Herman, A. L. Morrow, J. Besheer, T. L. Kash, C. A. Boettiger, D. L. Robinson, F. T. Crews, Y. I. Shih, An isotropic EPI database and analytical pipelines for rat brain resting-state fMRI. *Neuroimage* **243**, 118541 (2021).
34. A. Shatillo, A. Lipponen, R. A. Salo, H. Tanila, A. Verkhratsky, R. Giniatullin, O. H. Grohn, Spontaneous BOLD waves - A novel hemodynamic activity in Sprague-Dawley rat brain detected by functional magnetic resonance imaging. *J Cereb Blood Flow Metab* **39**, 1949-1960 (2019).
35. C. Nacif-Coelho, C. Correa-Sales, L. L. Chang, M. Maze, Perturbation of ion channel conductance alters the hypnotic response to the alpha 2-adrenergic agonist dexmedetomidine in the locus coeruleus of the rat. *Anesthesiology* **81**, 1527-1534 (1994).
36. Q. Wang, S. L. Ding, Y. Li, J. Royall, D. Feng, P. Lesnar, N. Graddis, M. Naeemi, B. Facer, A. Ho, T. Dolbeare, B. Blanchard, N. Dee, W. Wakeman, K. E. Hirokawa, A. Szafer, S. M. Sunkin, S. W. Oh, A. Bernard, J. W. Phillips, M. Hawrylycz, C. Koch, H. Zeng, J. A. Harris, L. Ng, The Allen Mouse Brain Common Coordinate Framework: A 3D Reference Atlas. *Cell* **181**, 936-953 e920 (2020).
37. E. A. Allen, E. B. Erhardt, E. Damaraju, W. Gruner, J. M. Segall, R. F. Silva, M. Havlicek, S. Rachakonda, J. Fries, R. Kalyanam, A. M. Michael, A. Caprihan, J. A. Turner, T. Eichele, S. Adelsheim, A. D. Bryan, J. Bustillo, V. P. Clark, S. W. Feldstein Ewing, F. Filbey, C. C. Ford, K. Hutchison, R. E. Jung, K. A. Kiehl, P. Kodituwakku, Y. M. Komesu, A. R. Mayer, G. D. Pearlson, J. P. Phillips, J. R. Sadek, M. Stevens, U. Teuscher, R. J. Thoma, V. D. Calhoun, A baseline for the multivariate comparison of resting-state networks. *Front Syst Neurosci* **5**, 2 (2011).
38. X. N. Zuo, C. Kelly, J. S. Adelstein, D. F. Klein, F. X. Castellanos, M. P. Milham, Reliable intrinsic connectivity networks: test-retest evaluation using ICA and dual regression approach. *Neuroimage* **49**, 2163-2177 (2010).

39. V. D. Blondel, J.-L. Guillaume, R. Lambiotte, E. Lefebvre, Fast unfolding of communities in large networks. *Journal of Statistical Mechanics: Theory and Experiment* **2008**, P10008 (2008).
40. Y. F. Zang, Y. He, C. Z. Zhu, Q. J. Cao, M. Q. Sui, M. Liang, L. X. Tian, T. Z. Jiang, Y. F. Wang, Altered baseline brain activity in children with ADHD revealed by resting-state functional MRI. *Brain Dev* **29**, 83-91 (2007).
41. D. Cordes, V. M. Haughton, K. Arfanakis, J. D. Carew, P. A. Turski, C. H. Moritz, M. A. Quigley, M. E. Meyerand, Frequencies contributing to functional connectivity in the cerebral cortex in "resting-state" data. *AJNR Am J Neuroradiol* **22**, 1326-1333 (2001).
42. W. Tu, Z. Ma, Y. Ma, D. Dopfel, N. Zhang, Suppressing Anterior Cingulate Cortex Modulates Default Mode Network and Behavior in Awake Rats. *Cereb Cortex* **31**, 312-323 (2021).
43. L. M. Peeters, R. Hinz, J. R. Detrez, S. Missault, W. H. De Vos, M. Verhoye, A. Van der Linden, G. A. Keliris, Chemogenetic silencing of neurons in the mouse anterior cingulate area modulates neuronal activity and functional connectivity. *Neuroimage* **220**, 117088 (2020).
44. T. J. M. Roelofs, J. P. H. Verharen, G. A. F. van Tilborg, L. Boekhoudt, A. van der Toorn, J. W. de Jong, M. C. M. Luijendijk, W. M. Otte, R. A. H. Adan, R. M. Dijkhuizen, A novel approach to map induced activation of neuronal networks using chemogenetics and functional neuroimaging in rats: A proof-of-concept study on the mesocorticolimbic system. *Neuroimage* **156**, 109-118 (2017).
45. A. Giorgi, S. Migliarini, A. Galbusera, G. Maddaloni, M. Mereu, G. Margiani, M. Gritti, S. Landi, F. Trovato, S. M. Bertozzi, A. Armirotti, G. M. Ratto, M. A. De Luca, R. Tonini, A. Gozzi, M. Pasqualetti, Brain-wide Mapping of Endogenous Serotonergic Transmission via Chemogenetic fMRI. *Cell Rep* **21**, 910-918 (2017).
46. S. P. Strebel, C. Kindler, B. Bissonnette, G. Tschaler, D. Deanovic, The impact of systemic vasoconstrictors on the cerebral circulation of anesthetized patients. *Anesthesiology* **89**, 67-72 (1998).
47. M. Michaelides, Y. L. Hurd, DREAMM: a biobehavioral imaging methodology for dynamic in vivo whole-brain mapping of cell type-specific functional networks. *Neuropsychopharmacology* **40**, 239-240 (2015).
48. N. Cannella, A. Cosa-Linan, M. Roscher, T. T. Takahashi, N. Vogler, B. Wangler, R. Spanagel, [18F]-Fluorodeoxyglucose-Positron Emission Tomography in Rats with Prolonged Cocaine Self-Administration Suggests Potential Brain Biomarkers for Addictive Behavior. *Front Psychiatry* **8**, 218 (2017).
49. J. D. Bremner, R. B. Innis, C. K. Ng, L. H. Staib, R. M. Salomon, R. A. Bronen, J. Duncan, S. M. Southwick, J. H. Krystal, D. Rich, G. Zubal, H. Dey, R. Soufer, D. S. Charney, Positron emission tomography measurement of cerebral metabolic correlates of yohimbine administration in combat-related posttraumatic stress disorder. *Arch Gen Psychiatry* **54**, 246-254 (1997).
50. A. Justice, S. M. Feldman, L. L. Brown, The nucleus locus coeruleus modulates local cerebral glucose utilization during noise stress in rats. *Brain Res* **490**, 73-84 (1989).

51. N. French, M. D. Lalies, D. J. Nutt, J. A. Pratt, Idazoxan-induced reductions in cortical glucose use are accompanied by an increase in noradrenaline release: complementary [14C]2-deoxyglucose and microdialysis studies. *Neuropharmacology* **34**, 605-613 (1995).
52. O. Sorg, P. J. Magistretti, Characterization of the glycogenolysis elicited by vasoactive intestinal peptide, noradrenaline and adenosine in primary cultures of mouse cerebral cortical astrocytes. *Brain Res* **563**, 227-233 (1991).
53. T. T. Quach, C. Rose, J. C. Schwartz, [3H]Glycogen hydrolysis in brain slices: responses to neurotransmitters and modulation of noradrenaline receptors. *J Neurochem* **30**, 1335-1341 (1978).
54. V. Menon, L. Q. Uddin, Saliency, switching, attention and control: a network model of insula function. *Brain Struct Funct* **214**, 655-667 (2010).
55. F. Mandino, R. M. Vrooman, H. E. Foo, L. Y. Yeow, T. A. W. Bolton, P. Salvan, C. L. Teoh, C. Y. Lee, A. Beauchamp, S. Luo, R. Bi, J. Zhang, G. H. T. Lim, N. Low, J. Sallet, J. Gigg, J. P. Lerch, R. B. Mars, M. Olivo, Y. Fu, J. Grandjean, A triple-network organization for the mouse brain. *Mol Psychiatry*, (2021).
56. H. J. Park, K. J. Friston, C. Pae, B. Park, A. Razi, Dynamic effective connectivity in resting state fMRI. *Neuroimage* **180**, 594-608 (2018).
57. R. M. Baron, D. A. Kenny, The moderator-mediator variable distinction in social psychological research: conceptual, strategic, and statistical considerations. *J Pers Soc Psychol* **51**, 1173-1182 (1986).
58. K. J. Preacher, A. F. Hayes, Asymptotic and resampling strategies for assessing and comparing indirect effects in multiple mediator models. *Behav Res Methods* **40**, 879-891 (2008).
59. J. D. Power, A. L. Cohen, S. M. Nelson, G. S. Wig, K. A. Barnes, J. A. Church, A. C. Vogel, T. O. Laumann, F. M. Miezin, B. L. Schlaggar, S. E. Petersen, Functional network organization of the human brain. *Neuron* **72**, 665-678 (2011).
60. M. Rubinov, Constraints and spandrels of interareal connectomes. *Nature communications* **7**, 13812 (2016).
61. L. M. Peeters, M. van den Berg, R. Hinz, G. Majumdar, I. Pintelon, G. A. Keliris, Cholinergic Modulation of the Default Mode Like Network in Rats. *iScience* **23**, 101455 (2020).
62. W. Tu, Z. Ma, Y. Ma, D. Dopfel, N. Zhang, Suppressing Anterior Cingulate Cortex Modulates Default Mode Network and Behavior in Awake Rats. *Cereb Cortex*, (2020).
63. J. Bonaventura, M. A. G. Eldridge, F. Hu, J. L. Gomez, M. Sanchez-Soto, A. M. Abramyan, S. Lam, M. A. Boehm, C. Ruiz, M. R. Farrell, A. Moreno, I. M. Galal Faress, N. Andersen, J. Y. Lin, R. Moaddel, P. J. Morris, L. Shi, D. R. Sibley, S. V. Mahler, S. Nabavi, M. G. Pomper, A. Bonci, A. G. Horti, B. J. Richmond, M. Michaelides, High-potency ligands for DREADD imaging and activation in rodents and monkeys. *Nature communications* **10**, 4627 (2019).
64. B. L. Roth, DREADDs for Neuroscientists. *Neuron* **89**, 683-694 (2016).
65. J. L. Gomez, J. Bonaventura, W. Lesniak, W. B. Mathews, P. Sysa-Shah, L. A. Rodriguez, R. J. Ellis, C. T. Richie, B. K. Harvey, R. F. Dannals, M. G. Pomper, A. Bonci, M. Michaelides, Chemogenetics revealed: DREADD occupancy and activation via converted clozapine. *Science* **357**, 503-507 (2017).

66. N. K. Logothetis, What we can do and what we cannot do with fMRI. *Nature* **453**, 869-878 (2008).
67. L. K. Bekar, H. S. Wei, M. Nedergaard, The locus coeruleus-norepinephrine network optimizes coupling of cerebral blood volume with oxygen demand. *J Cereb Blood Flow Metab* **32**, 2135-2145 (2012).
68. M. E. Raichle, B. K. Hartman, J. O. Eichling, L. G. Sharpe, Central noradrenergic regulation of cerebral blood flow and vascular permeability. *Proc Natl Acad Sci U S A* **72**, 3726-3730 (1975).
69. R. L. van den Brink, T. Pfeffer, C. M. Warren, P. R. Murphy, K. D. Tona, N. J. van der Wee, E. Giltay, M. S. van Noorden, S. A. Rombouts, T. H. Donner, S. Nieuwenhuis, Catecholaminergic Neuromodulation Shapes Intrinsic MRI Functional Connectivity in the Human Brain. *J Neurosci* **36**, 7865-7876 (2016).
70. E. M. Vazey, D. E. Moorman, G. Aston-Jones, Phasic locus coeruleus activity regulates cortical encoding of salience information. *Proc Natl Acad Sci U S A* **115**, E9439-E9448 (2018).
71. K. Koga, A. Yamada, Q. Song, X. H. Li, Q. Y. Chen, R. H. Liu, J. Ge, C. Zhan, H. Furue, M. Zhuo, T. Chen, Ascending noradrenergic excitation from the locus coeruleus to the anterior cingulate cortex. *Mol Brain* **13**, 49 (2020).
72. R. M. Neves, S. van Keulen, M. Yang, N. K. Logothetis, O. Eschenko, Locus coeruleus phasic discharge is essential for stimulus-induced gamma oscillations in the prefrontal cortex. *J Neurophysiol* **119**, 904-920 (2018).
73. X. Toussay, K. Basu, B. Lacoste, E. Hamel, Locus coeruleus stimulation recruits a broad cortical neuronal network and increases cortical perfusion. *J Neurosci* **33**, 3390-3401 (2013).
74. J. M. Shine, R. L. van den Brink, D. Hernaus, S. Nieuwenhuis, R. A. Poldrack, Catecholaminergic manipulation alters dynamic network topology across cognitive states. *Netw Neurosci* **2**, 381-396 (2018).
75. E. Eldar, J. D. Cohen, Y. Niv, The effects of neural gain on attention and learning. *Nat Neurosci* **16**, 1146-1153 (2013).
76. A. T. Baria, M. N. Baliki, T. Parrish, A. V. Apkarian, Anatomical and functional assemblies of brain BOLD oscillations. *J Neurosci* **31**, 7910-7919 (2011).
77. C. Grefkes, L. E. Wang, S. B. Eickhoff, G. R. Fink, Noradrenergic modulation of cortical networks engaged in visuomotor processing. *Cereb Cortex* **20**, 783-797 (2010).
78. M. Mittner, W. Boekel, A. M. Tucker, B. M. Turner, A. Heathcote, B. U. Forstmann, When the brain takes a break: a model-based analysis of mind wandering. *J Neurosci* **34**, 16286-16295 (2014).
79. F. A. Picon, J. R. Sato, M. Anes, L. M. Vedolin, A. A. Mazzola, B. B. Valentini, R. B. Cupertino, R. G. Karam, M. M. Victor, V. Breda, K. Silva, N. da Silva, Jr., C. H. D. Bau, E. H. Grevet, L. A. P. Rohde, Methylphenidate Alters Functional Connectivity of Default Mode Network in Drug-Naive Male Adults With ADHD. *J Atten Disord* **24**, 447-455 (2020).
80. M. Wang, B. P. Ramos, C. D. Paspalas, Y. Shu, A. Simen, A. Duque, S. Vijayraghavan, A. Brennan, A. Dudley, E. Nou, J. A. Mazer, D. A. McCormick, A. F. Arnsten, Alpha2A-adrenoceptors strengthen working memory networks by inhibiting cAMP-HCN channel signaling in prefrontal cortex. *Cell* **129**, 397-410 (2007).

81. C. Andreescu, M. Wu, M. A. Butters, J. Figurski, C. F. Reynolds, 3rd, H. J. Aizenstein, The default mode network in late-life anxious depression. *Am J Geriatr Psychiatry* **19**, 980-983 (2011).
82. F. Saviola, E. Pappaianni, A. Monti, A. Grecucci, J. Jovicich, N. De Pisapia, Trait and state anxiety are mapped differently in the human brain. *Sci Rep* **10**, 11112 (2020).
83. M. E. Carter, O. Yizhar, S. Chikahisa, H. Nguyen, A. Adamantidis, S. Nishino, K. Deisseroth, L. de Lecea, Tuning arousal with optogenetic modulation of locus coeruleus neurons. *Nat Neurosci* **13**, 1526-1533 (2010).
84. D. J. Chandler, Evidence for a specialized role of the locus coeruleus noradrenergic system in cortical circuitries and behavioral operations. *Brain Res* **1641**, 197-206 (2016).
85. C. Zarow, S. A. Lyness, J. A. Mortimer, H. C. Chui, Neuronal loss is greater in the locus coeruleus than nucleus basalis and substantia nigra in Alzheimer and Parkinson diseases. *Arch Neurol* **60**, 337-341 (2003).
86. Y. Sawada, Y. Nishio, K. Suzuki, K. Hirayama, A. Takeda, Y. Hosokai, T. Ishioka, Y. Itoyama, S. Takahashi, H. Fukuda, E. Mori, Attentional set-shifting deficit in Parkinson's disease is associated with prefrontal dysfunction: an FDG-PET study. *PLoS One* **7**, e38498 (2012).
87. A. Mohan, A. J. Roberto, A. Mohan, A. Lorenzo, K. Jones, M. J. Carney, L. Liogier-Weyback, S. Hwang, K. A. Lapidus, The Significance of the Default Mode Network (DMN) in Neurological and Neuropsychiatric Disorders: A Review. *Yale J Biol Med* **89**, 49-57 (2016).
88. A. C. Peterson, C. R. Li, Noradrenergic Dysfunction in Alzheimer's and Parkinson's Diseases-An Overview of Imaging Studies. *Front Aging Neurosci* **10**, 127 (2018).
89. A. Bari, S. Xu, M. Pignatelli, D. Takeuchi, J. Feng, Y. Li, S. Tonegawa, Differential attentional control mechanisms by two distinct noradrenergic coeruleo-frontal cortical pathways. *Proc Natl Acad Sci U S A* **117**, 29080-29089 (2020).
90. R. A. Kimmel, D. H. Turnbull, V. Blanquet, W. Wurst, C. A. Loomis, A. L. Joyner, Two lineage boundaries coordinate vertebrate apical ectodermal ridge formation. *Genes Dev* **14**, 1377-1389 (2000).
91. N. W. Plummer, I. Y. Evsyukova, S. D. Robertson, J. de Marchena, C. J. Tucker, P. Jensen, Expanding the power of recombinase-based labeling to uncover cellular diversity. *Development* **142**, 4385-4393 (2015).
92. M. Das, E. A. Oyarzabal, L. Chen, S. H. Lee, N. Shah, G. Gerlach, W. Zhang, T. H. Chao, N. V. D. Berge, C. Liu, C. Donley, S. A. Montgomery, Y. I. Shih, One-pot synthesis of carboxymethyl-dextran coated iron oxide nanoparticles (CION) for preclinical fMRI and MRA applications. *Neuroimage* **238**, 118213 (2021).
93. L. M. Hsu, S. Wang, P. Ranadive, W. Ban, T. H. Chao, S. Song, D. H. Cerri, L. R. Walton, M. A. Broadwater, S. H. Lee, D. Shen, Y. I. Shih, Automatic Skull Stripping of Rat and Mouse Brain MRI Data Using U-Net. *Front Neurosci* **14**, 568614 (2020).
94. V. Zerbi, J. Grandjean, M. Rudin, N. Wenderoth, Mapping the mouse brain with rs-fMRI: An optimized pipeline for functional network identification. *Neuroimage* **123**, 11-21 (2015).
95. M. Rubinov, O. Sporns, Weight-conserving characterization of complex functional brain networks. *Neuroimage* **56**, 2068-2079 (2011).

96. H. Lv, Z. Wang, E. Tong, L. M. Williams, G. Zaharchuk, M. Zeineh, A. N. Goldstein-Piekarski, T. M. Ball, C. Liao, M. Wintermark, Resting-State Functional MRI: Everything That Nonexperts Have Always Wanted to Know. *AJNR Am J Neuroradiol* **39**, 1390-1399 (2018).
97. A. Zalesky, A. Fornito, E. T. Bullmore, Network-based statistic: identifying differences in brain networks. *Neuroimage* **53**, 1197-1207 (2010).
98. W. D. Penny, K. E. Stephan, J. Daunizeau, M. J. Rosa, K. J. Friston, T. M. Schofield, A. P. Leff, Comparing families of dynamic causal models. *PLoS Comput Biol* **6**, e1000709 (2010).
99. A. Boucard, A. Marchand, X. Nogues, Reliability and validity of structural equation modeling applied to neuroimaging data: a simulation study. *J Neurosci Methods* **166**, 278-292 (2007).
100. C. A. S. Stone, M.E., The robustness of estimates of total indirect effects in covariance structure models estimated by maximum. *Psychometrika* **55**, 337–352 (1990).

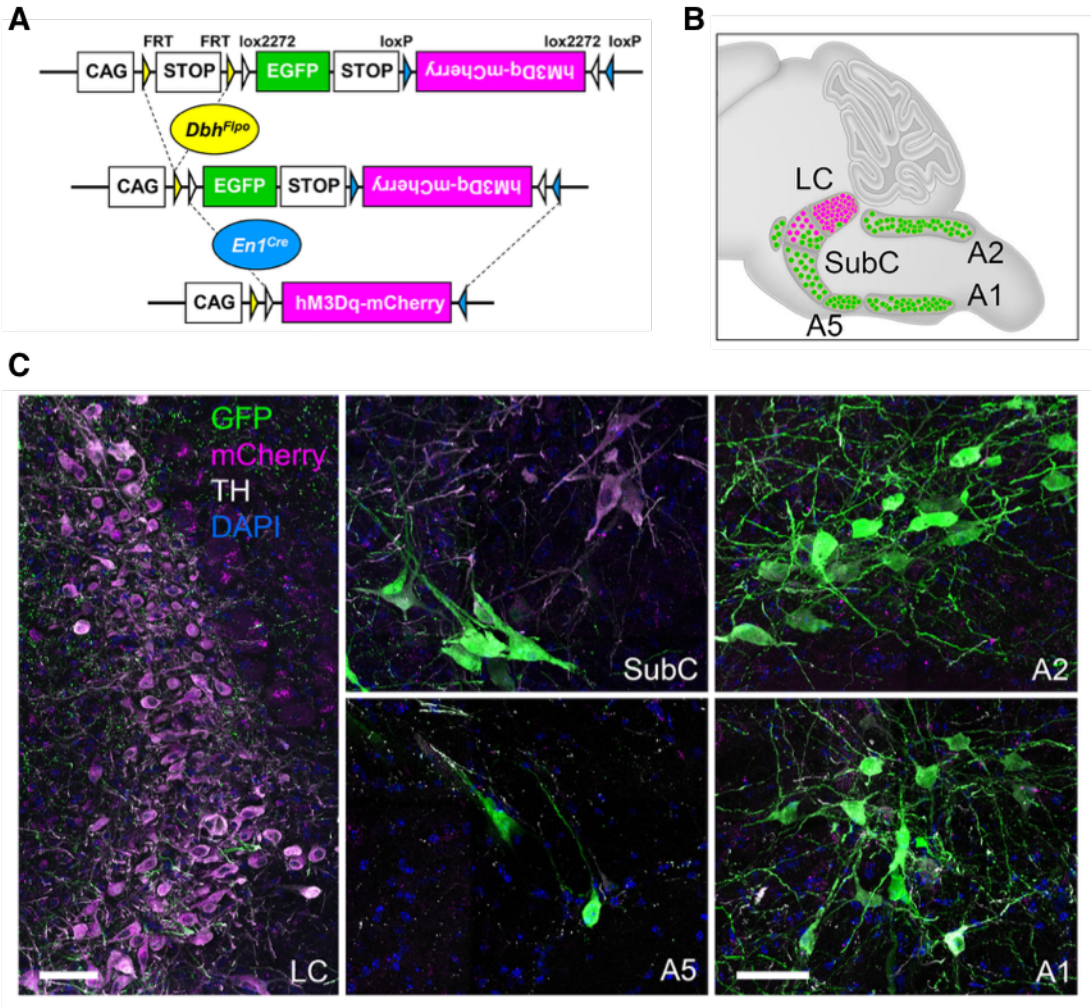

Fig 1. Intersectional chemogenetic strategy to selectively activate LC-NE neurons. (A) Schematic illustration of the intersectional genetic strategy. **(B)** A sagittal schematic diagram of the hindbrain compressed along the mediolateral axis illustrates the approximate position of NE neurons. Recombination of the RC::FL-hM3Dq allele by the noradrenergic-specific driver *Dbh*^{Flpo} and *En1*^{cre} results in expression of the excitatory G-protein-coupled receptor hM3Dq fused to mCherry in LC-NE neurons (magenta cells in schematic). Expression of *Dbh*^{Flp} by all remaining NE neurons results in expression of GFP(green neurons in schematic). **(C)** Immunofluorescent labeling of sections from the adult brainstem of LC-NE/hM3Dq mice reveals hM3Dq-mCherry-expressing NE neurons in the LC (magenta) and GFP-expressing NE neurons (green) in the SubC, A5, and C2/A2, and C1/A1 nuclei. Scale bar indicates 50 µm.

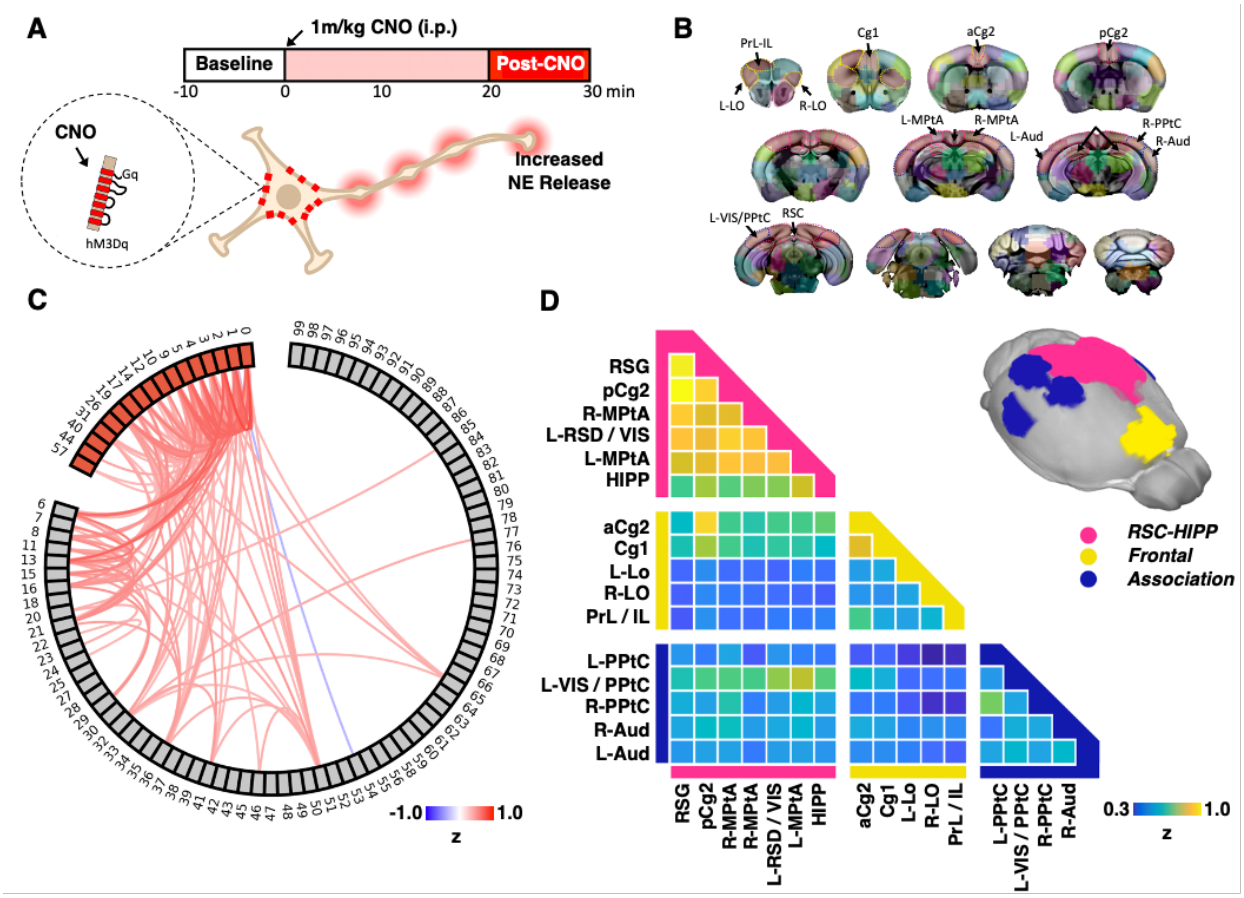

Fig. 2 Experimental design and identification of mouse DMN modules. (A) Experimental design includes a 10 min baseline prior to CNO administration and 30 min of scans after CNO. **(B)** 100 ICs were derived from group ICA of baseline scans among all subjects and DMN ICs were anatomically specified with respect to established brain regions found in canonical rodent DMN. **(C)** Correlation among the 100 ICs were plotted with a threshold Fischer | z | > 0.3. DMN ICs were labeled in red. **(D)** Modularity analysis of DMN ICs shows that the mouse DMN comprises of a Frontal (yellow), an *RSC-HIPP* (pink), and an *Association* module (blue).

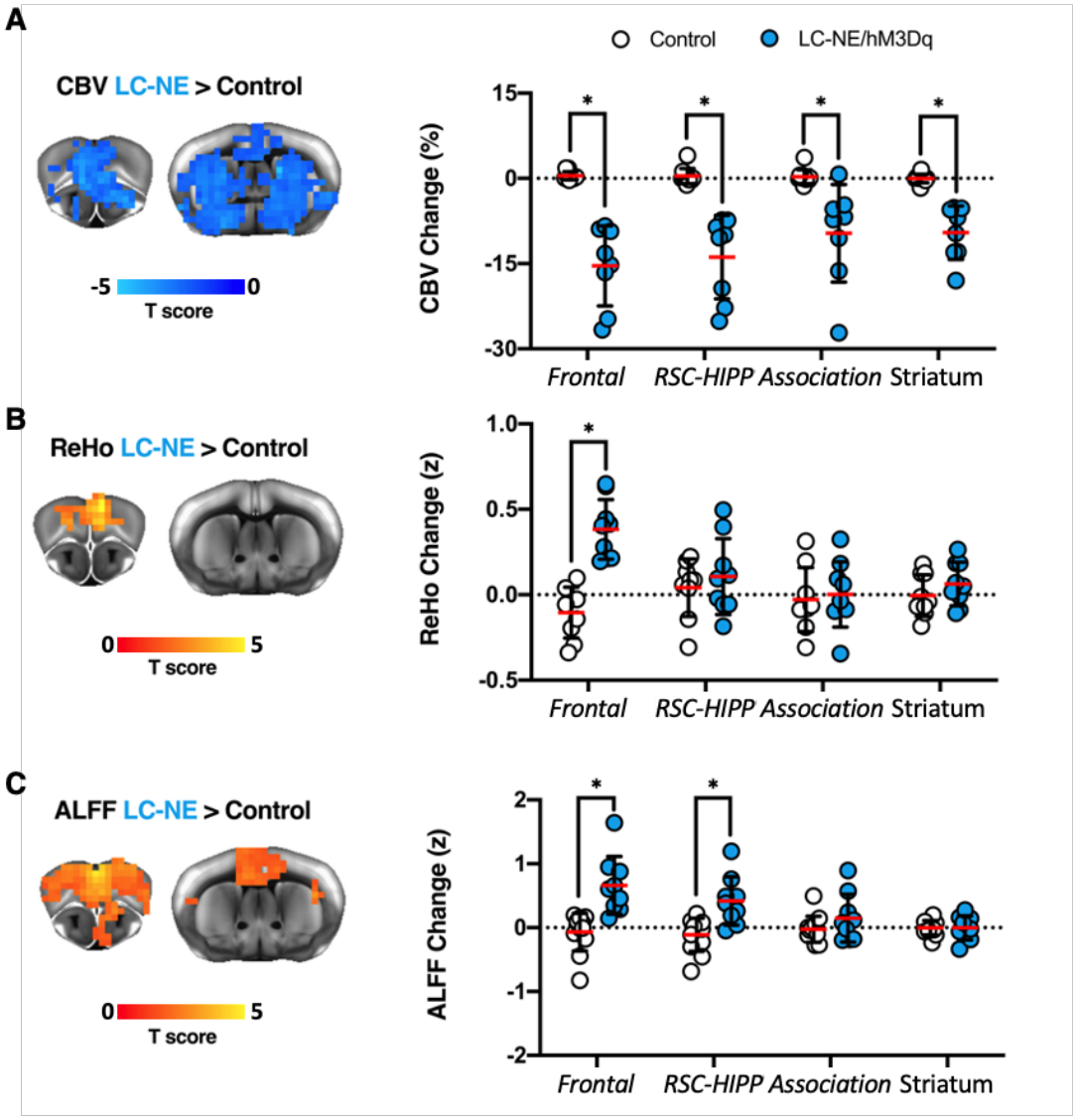

Fig. 3 CBV, ReHo, and ALFF changes in DMN modules following activation of LC-NE neurons. (A) CBV decreased significantly following LC-NE release across all DMN modules compared to baseline and controls. LC-NE release significantly increased **(B)** ReHo in the *Frontal* DMN module and **(C)** ALFF in *Frontal* and *RSC-HIPP* modules compared to baseline and controls. * $p < 0.05$, ** $p < 0.0001$, red horizontal lines present means, and error bars represent ± SD.

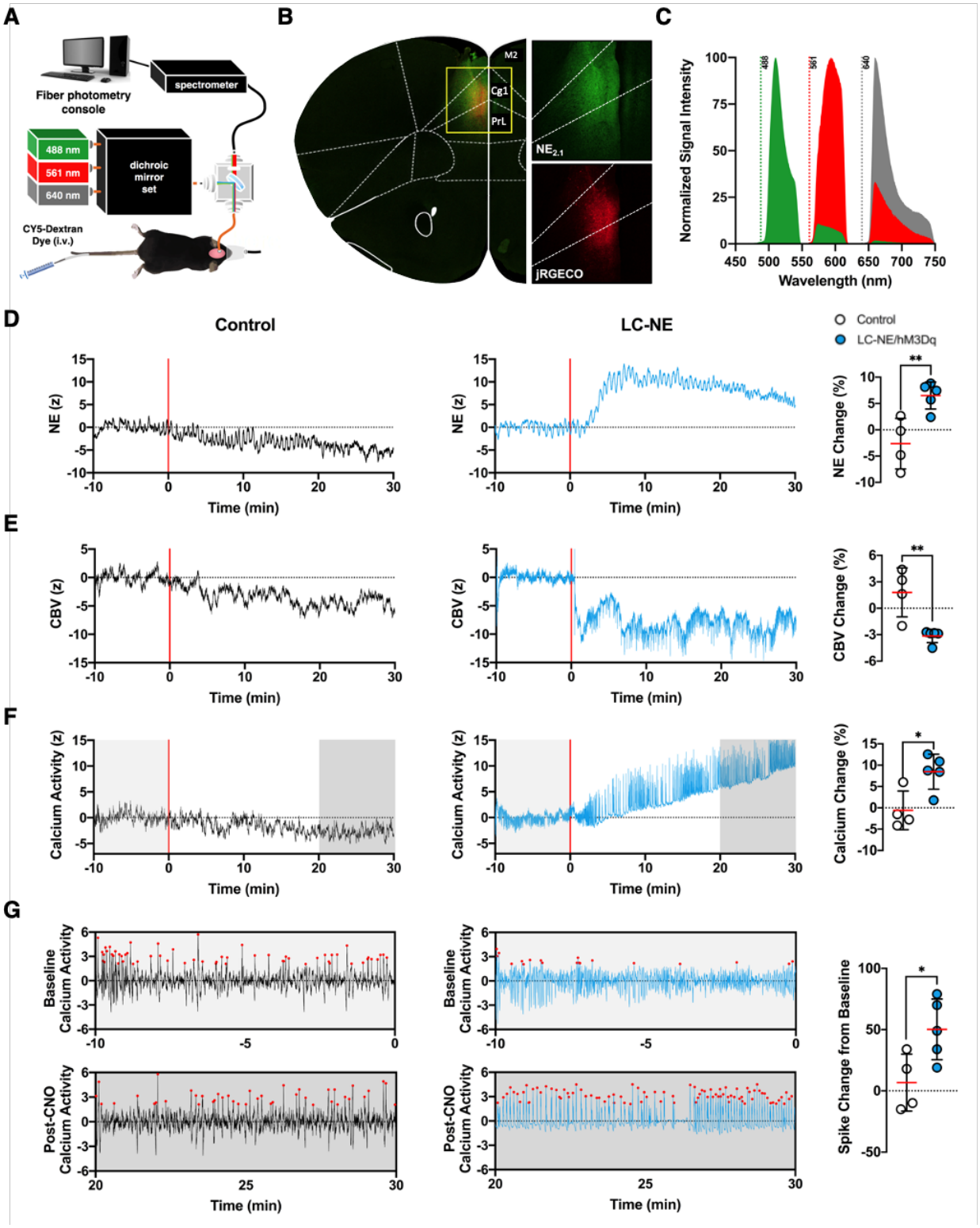

Fig. 4 Triple-spectral fiber photometry measuring NE release, CBV, and calcium-weighted neuronal activity in Cg1. (A) Experimental setup of the fiber-photometry system with 488, 561 and 640 nm lasers simultaneously used to detect NE release ($NE_{2.1}$), neuronal calcium activity

(jRGECO1a), and CBV (CY5-Dextran dye) changes, respectively. **(B)** Cg1 neurons were confirmed to be transfected to express $NE_{2.1}$ (green) and jRGECO1a (red) sensors. **(C)** Spectral profiles of NE neuronal activity and CBV sensors emission used to resolve signals via an established spectral unmined approach. **(D-F)** Respective effects of CNO on NE release, CBV, and neuronal activity in Cg1 from representative subjects and group level bar graphs. **(G)** CNO-induced LC-NE activation altered post-synaptic calcium spiking pattern, resulting in a significant increase in spike counts. * $p < 0.05$, ** $p < 0.01$, red horizontal lines present means, and error bars represent ± SD.

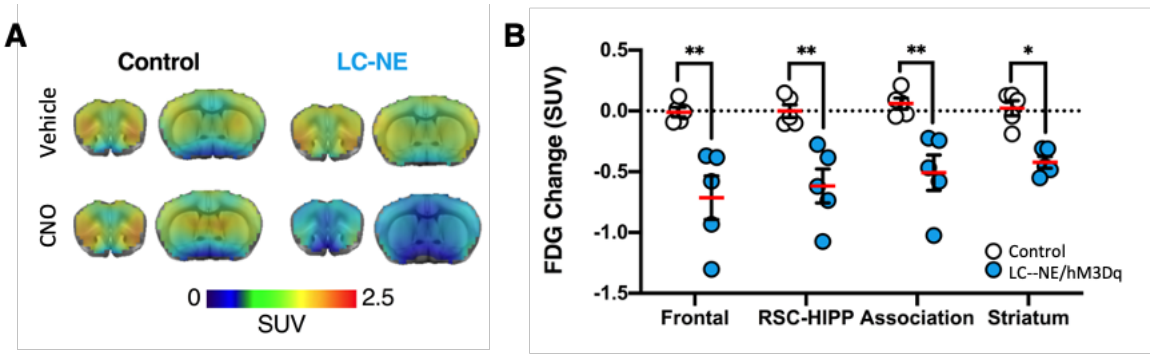

Fig. 5 Glucose uptake changes in DMN modules brain wide following activation of LC-NE neurons. **(A)** Activation of LC-NE neurons significantly decreased FDG uptake compared to saline-treated sham and littermate controls receiving CNO **(B)** Significant reduction in difference in standard uptake values (SUV) in all DMN regions. SUV changes were derived from each subject underwent two scans (vehicle and CNO administration) following co-registration. Comparisons were made against littermate controls. * $p < 0.001$, ** $p < 0.0001$, red horizontal lines present means, and error bars represent ± SD.

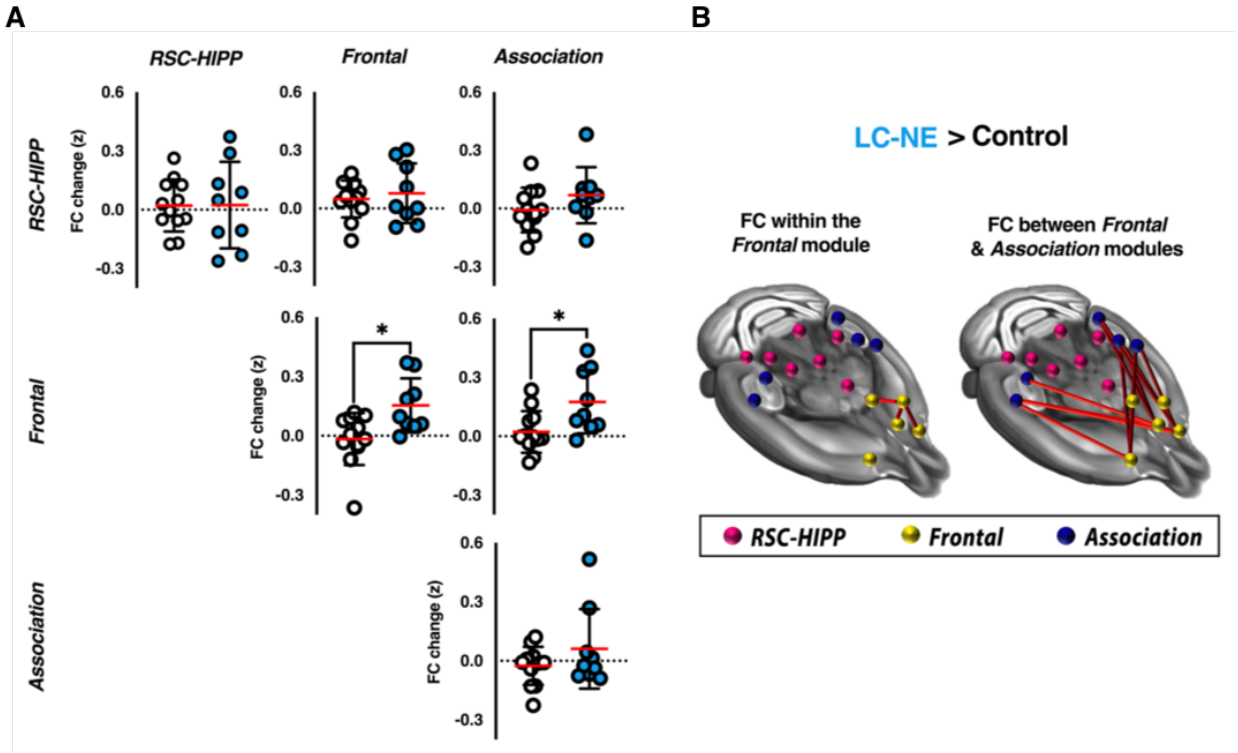

Fig. 6 FC changes among DMN modules following activation of LC-NE neurons. (A) Within and between DMN module FC changes. **(B)** Network-based statistical analysis showing significant differences in FC among edges in LC-NE > Control. * $P_{\text{FDR-corrected}} < 0.01$, red horizontal lines present means, and error bars represent ± SD.

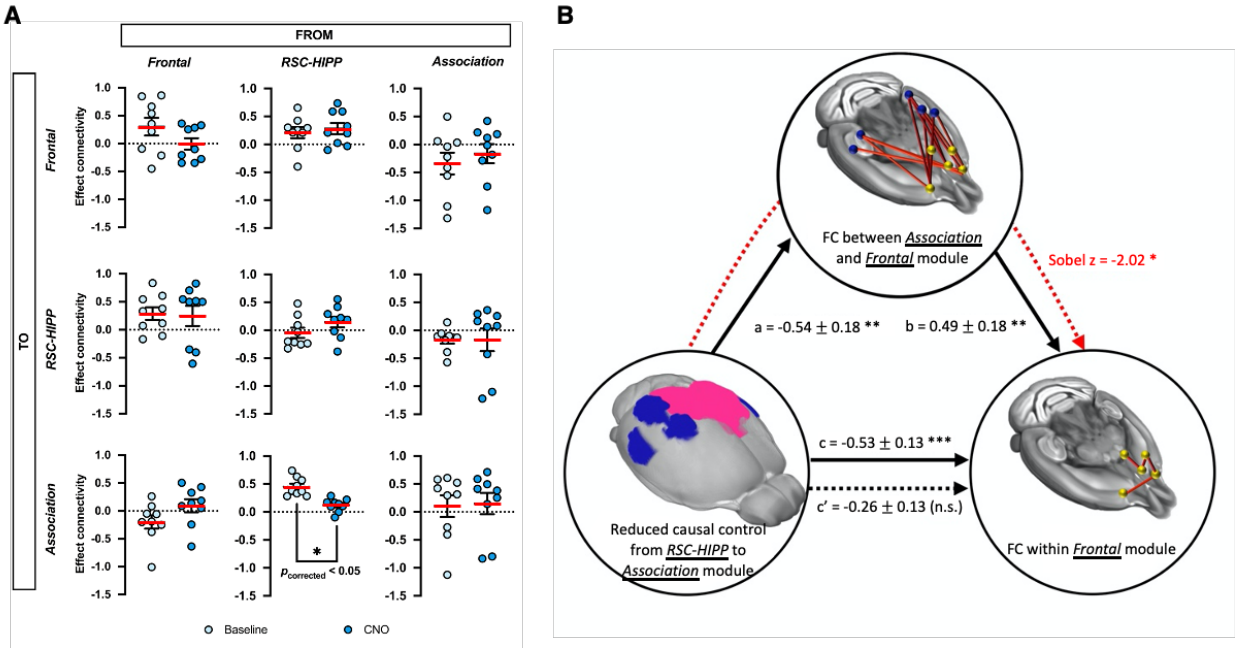

Fig. 7 DCM and mediation analysis among DMN modules. (A) DCM analysis among DMN modules found that *RSC-HIPP* reduced its causal modulation to the *Association* module upon LC-NE activation ($P_{FDR\text{-}corrected}$<0.05, red horizontal lines present means, and error bars represent ± SD.). **(B)** Mediation analysis was performed with direct effect (a, b, c) and with a mediator (c'). A Sobel test was also performed (red dot line) to evaluate the significance of mediation effect (Sobel z-value = -2.02, $P < 0.05$). * $P < 0.05$, ** $P < 0.01$, *** $P < 0.001$, n.s. = no significance.